

Review

# The Effect of Reduction and Oxidation Processes on the Work Function of Metal Oxide Crystals: TiO<sub>2</sub>(110) and SrTiO<sub>3</sub>(001) Case

Karol Cieřlik <sup>1,2,\*</sup>, Dominik Wrana <sup>1</sup>, Maciej Rogala <sup>3</sup> , Christian Rodenbuecher <sup>4</sup> , Krzysztof Szot <sup>5</sup> and Franciszek Krok <sup>1</sup>

<sup>1</sup> Marian Smoluchowski Institute of Physics, Jagiellonian University, Lojasiewicza 11, 30-348 Krakow, Poland; dominik.wrana@uj.edu.pl (D.W.); franciszek.krok@uj.edu.pl (F.K.)

<sup>2</sup> Institute of Applied Physics, Justus Liebig University Giessen, Heinrich-Buff-Ring 16, 35392 Giessen, Germany

<sup>3</sup> Department of Solid State Physics, Faculty of Physics and Applied Informatics, University of Lodz, Pomorska 149/153, 90-236 Lodz, Poland; maciej.rogala@uni.lodz.pl

<sup>4</sup> Institute of Energy and Climate Research (IEK-14), Forschungszentrum Juelich GmbH, 52425 Juelich, Germany; c.rodenbuecher@fz-juelich.de

<sup>5</sup> A. Chełkowski Institute of Physics, University of Silesia, 41-500 Chorzów, Poland; krzysztof.szot@us.edu.pl

\* Correspondence: karol.cieslik@ap.physik.uni-giessen.de

**Abstract:** The strict control of the work function of transition metal oxide crystals is of the utmost importance not only to fundamental research but also to applications based on these materials. Transition metal oxides are highly abundant in electronic devices, as their properties can be easily modified using redox processes. However, this ease of tuning is a double-edged sword. With the ease of manipulation comes difficulty in controlling the corresponding process. In this study, we demonstrate how redox processes can be induced in a laboratory setting and how they affect the work function of two model transition metal oxide crystals, namely titanium dioxide TiO<sub>2</sub>(110) and strontium titanate SrTiO<sub>3</sub>(001). To accomplish this task, we utilized Kelvin Probe Force Microscopy (KPFM) to monitor changes in work function, Scanning Tunneling Microscopy (STM), and Low-Energy Electron Diffraction (LEED) to check the surface morphology and reconstruction, and we also used X-ray Photoelectron Spectroscopy (XPS) to determine how the surface composition evolves. We also show that using redox processes, the work function of titanium dioxide can be modified in the range of 3.4–5.0 eV, and that of strontium titanate can be modified in the range of 2.9–4.5 eV. Moreover, we show that the presence of an oxygen-gaining material in the vicinity of a transition metal oxide during annealing can deepen the changes to its stoichiometry and therefore the work function.

**Keywords:** oxide; reduction; oxidation; work function; TiO<sub>2</sub>; SrTiO<sub>3</sub>; perovskites; surfaces; KPFM; STM; LEED



**Citation:** Cieřlik, K.; Wrana, D.; Rogala, M.; Rodenbuecher, C.; Szot, K.; Krok, F. The Effect of Reduction and Oxidation Processes on the Work Function of Metal Oxide Crystals: TiO<sub>2</sub>(110) and SrTiO<sub>3</sub>(001) Case. *Crystals* **2023**, *13*, 1052. <https://doi.org/10.3390/cryst13071052>

Academic Editor: Pier Carlo Ricci

Received: 11 June 2023

Revised: 27 June 2023

Accepted: 30 June 2023

Published: 3 July 2023



**Copyright:** © 2023 by the authors. Licensee MDPI, Basel, Switzerland. This article is an open access article distributed under the terms and conditions of the Creative Commons Attribution (CC BY) license (<https://creativecommons.org/licenses/by/4.0/>).

## 1. Introduction

Rapid development in the fields of electronic devices and renewable energy sources has led to an increase in demand for materials with tailored electronic properties. One class of materials that has attracted considerable attention in this context is transition metal oxides. These materials exhibit a wide range of electronic and optical properties, making them promising candidates for many applications, including solar cells [1–3], sensors [4], photocatalysts [5–8], and storage systems [9,10]. An important electronic property that is especially relevant in the field of electronic devices is the work function of a given material.

The work function is a quantitative measure of the energy required to remove an electron from the Fermi level to the vacuum one. A material's work function determines its ability to emit and receive electrons, making it a critical parameter for devices such as

transistors and solar cells. In this context, research has focused on understanding and controlling the work function of metal oxides through various processing techniques, including reduction and oxidation processes. These processes can modify the surface chemistry and electronic structure of the oxide, altering its work function and other electronic properties. Crystals can be reduced using many means, e.g., by annealing in vacuum conditions [11], sputtering [12], using direct current [13], electron irradiation [14], or chemical methods [15]. The investigation reported in this paper will employ reduction by thermal annealing, sputtering, and the combination of the two approaches. The work function can also be modified by the opposite reaction to reduction, namely oxidation. In this study, oxidation was facilitated by exposing the surface to oxygen at room temperature. Before considering the effects of each of these methods of inducing redox processes on work functions, it is beneficial to consider how each of them affects the crystal at the atomic scale.

The following processes occur during thermal reduction: oxygen atoms exit the crystal, and the excess titanium atoms move into interstitial positions [16], which leads to a reduction in the crystal. The greatest reduction in the surface, however, occurs not at high temperatures during annealing but during the cooling process [17]. This surprising process is caused by differences in the defect formation energy between the bulk at high temperatures and that at low temperatures. At elevated temperatures, oxygen effuses from the crystal's surface but also flows from the bulk to the surface, which is driven by the lower vacancy formation on the surface. However, the energy of oxygen vacancy formation is a function of temperature [17], and during cooling, a diffusion of vacancies to the surface occurs, leading to changes from the ratio of vacancies on the surface to those in the bulk that is equal to 1.2 at 1100 °C, to 6.7 during cooling [17].

The sputtering of crystals using ion beams is a time-tested technique that has been used in surface science laboratories in many ways: as part of cleaning procedures [18], as a means of creating nanostructures [19], or as a way to implant dopants [20]. It is fairly intrusive and changing, as it leads to the scattering of components and roughening of surfaces, and, in the case of oxides, it also reduces the crystals. TiO<sub>2</sub> has been used to create a highly conductive suboxide layer on the surface of the crystal [21] or even to form a layer of TiO beneath it [22]. Irradiation with an energetic ion beam of a system composed of different elements may lead to changes in its composition due to preferential sputtering, i.e., one projectile from the ion beam has a higher probability of removing one of the components than the other. This ballistic process has been observed experimentally in oxides [12] and, in the case of TiO<sub>2</sub>, the sputtering ratio is 1.3 [23], with more oxygen being sputtered per projectile than titanium atoms.

Reduced crystals can be reoxidized in Ultra-High Vacuum (UHV) conditions at elevated temperatures in the presence of gaseous oxygen. In such cases, oxidation of the reduced TiO<sub>2</sub> occurs via the diffusion of Ti<sup>3+</sup> from the bulk to the surface, where it reacts with atmospheric oxygen [16]. It has been proposed that the process of reoxidation likely begins at shear planes, which are the nucleation sites for oxidation [24]. The regrowth of the surface occurs with new layers of TiO<sub>2</sub> forming consecutively on the surface of the crystal until stoichiometry is reached. This process is highly dependent on temperature, with significant rates of reoxidation observed experimentally at temperatures from 300 to 800 °C. Reoxidation also occurs at lower temperatures but at much slower rates [16]. Annealing in oxygen-rich conditions further oxidizes the crystal [25], but the process also brings about changes in the surface [26,27]. Under such conditions, the reaction of interstitial titanium and gaseous oxygen leads to the formation of rosettes, strands, and islands [26,27]. These structures are respectively composed of incomplete TiO<sub>2</sub> layers, Ti<sub>2</sub>O<sub>3</sub>, and small (1 × 1) islands [27]. Furthermore, the process of oxidation at elevated temperatures is not limited to the surface, as oxygen diffuses into the crystal's bulk in the form of oxygen interstitials at high temperatures and annihilates vacancies present below the surface [28].

The reported values of work function vary greatly in the published articles. A case in point is the widely studied titanium dioxide (110) surface. The range of values reported for stoichiometric TiO<sub>2</sub>(110) surfaces, i.e., 5.2 eV [29], 5.3 eV [30], 5.35 eV [31], 5.5 eV [32] and

5.5 eV to 5.8 eV [33]. The wide distribution of values has been explained by the differences in the defect densities on the surfaces, with the work function decreasing with increasing defect coverages [33]. What is telling is the fact that Onda et al. (2004) [33] reported that in their experiments, following the same preparation method, they saw variability in the work function, in the range of 5.5 to 5.8 eV, so there must be some variability in the monocrystals themselves. The fact that the leveling-off value of the work function is so close to the stoichiometric values shows that sample preparation using many cleaning cycles allows, in the case of the work function, to obtain a surface which is very close to the stoichiometric one.

Work function can be measured in many ways—for example, using Kelvin Probe Force Microscopy (KPFM), as in this publication, but also using techniques such as Scanning Auger Microprobe (SAM) [34] and ultraviolet photoelectron spectroscopy (UPS) [25]. The values obtained from the same sample using different methods might be different. In case of UPS, if the studied surface is composed of different components with different work functions [35,36], the high work function region creates an additional barrier for electrons leaving the low work function regions, which increases the measured work function [35,36]. In case of KPFM there is no such difficulty; however, careful calibration is required before and after each measurement to transform the measured contact potential difference maps into work function maps.

Monocrystals can also be oxidized at much lower temperatures. The healing of surface oxygen vacancies begins at a temperature of 120 K [37]. Oxidation in such conditions heals some surface oxygen vacancies, but even at room temperature, not all vacancies will be healed [17,38]. Additionally, such oxidation does not affect the non-stoichiometry below the surface, as high temperatures are necessary for that to occur [28]. A method for obtaining a TiO<sub>2</sub> surface that is close to stoichiometric plasma cleaning has been deemed the best [25,39], as oxygen plasma is more oxidative than molecular oxygen. Moreover, this method does not require high temperatures, which prevents the segregation of impurities on the surface (as is the case, e.g., with iron in anatase [40] or calcium in rutile [41]).

Titanium dioxide is a ubiquitous compound whose annual production is estimated at 5 and 10 million tonnes [42]. It is mostly used as a pigment for paints, coatings, paper etc. [42], due to its exceptionally high refractive index (2.73 for rutile [43]). Nanoparticles of TiO<sub>2</sub> are used in other fields, such as catalysis and electroceramics, and even in sunscreens [42]. Moreover, its exceptional properties and its easy manipulation make titanium dioxide an attractive compound for high-tech applications from photocatalysts [44,45], and self-cleaning paints [46], to memristors [10].

Strontium titanate first entered the application stage as a diamond substitute in 1951 [47]; however, its usage has shifted from jewelry applications to sophisticated technologies. This compound can be used as a highly stable electron transport layer in solar cells [2], as a model memristor [48], as a high-energy storage device [49], as a photocatalyst [7], or in Radio Frequency (RF) circuits [50]. Moreover, SrTiO<sub>3</sub> is widely used as a growth substrate of thin films of perovskite materials, including materials exhibiting superconductivity [51,52]. It is an extensively studied material considered a model perovskite crystal [53,54] as well as a model ternary oxide [55].

The goal of investigating reduction and oxidation processes on TiO<sub>2</sub>(110) and SrTiO<sub>3</sub>(001) surfaces is to understand the fundamental mechanisms underlying the electronic properties of these materials and develop strategies for tailoring them to specific device applications. This is especially important given that commonly used physical methods for obtaining the defined and stoichiometric surfaces of these oxides (e.g., temperature annealing, ion-beam sputtering, or crystal breaking) result in surfaces with different amounts of point defects and values of the work function. For example, depending on the sample and preparation, the work function of anatase (001) may vary in the range of 3.61 to 6.76 eV [56]. Most of the data presented in this paper were acquired within our group and complemented by some literature results.

## 2. Materials and Methods

### 2.1. Experimental Techniques

The Scanning Probe Microscopy (SPM) measurements were performed in UHV using the room temperature Omicron microscope with Atomic Force Microscopy (AFM) and Scanning Tunneling Microscope (STM) capabilities. Chemically etched tungsten tips were used for the STM measurements, whereas PPP-contPt cantilevers (Pt-Ir coated with an eigenfrequency of 17 kHz) were utilized for Kelvin Probe Force Microscopy (KPFM) investigations. For KPFM measurements, non-contact AFM Pt-Ir-coated tips were also occasionally used. To analyze the long-range atomic arrangement of the surfaces, a Low-Energy Electron Diffraction (LEED)/Auger Electron Spectroscopy device equipped with a microchannel plate (OCI Vacuum Microengineering Inc., London, ON, Canada) was employed. To verify the stoichiometric composition, the X-ray Photoelectron Spectroscopy (XPS) spectra were collected using a Phoibos 150 (SPECS) spectrometer with a 2D-CCD detector equipped with the DAR 500 X-ray lamp with non-monochromatic radiation (1253.64 eV Mg K $\alpha$ ).

### 2.2. KPFM Calibration

Kelvin Probe Force Microscopy measurements to provide the contact potential maps were performed simultaneously with the standard topography measurements, which was made possible by using the additional third loop for sample bias compensation [40,57]. The contact PPP-contPt tips were used in most of the experiments, even though KPFM is a non-contact mode because the tip was excited to higher harmonics (approximately 90 kHz). The amplitude of oscillation was approximately 10 nm. The bias loop operated with the modulation sample bias frequency of 100–200 Hz, and the amplitude was 500 mV. To obtain absolute work function values, the tips were calibrated before and after measurements against the highly oriented pyrolytic graphite (HOPG) surface, which has a well-known work function of 4.5 eV [41,42].

### 2.3. Experiments in the Effects of Sputtering

To systematically study the changes brought about by sputtering, two types of experiments were performed: changing the ion beam fluence at a constant energy of ions and changing energy at a constant ion beam fluence. To study the effect of fluence, the sample was fully masked and the ion gun was turned on with an energy of 2 keV. Subsequently, the sample was gradually unmasked, resulting in a gradient of fluency. The fluences studied were in the range of  $5 \times 10^{15}$  ions/cm<sup>2</sup> to  $1.2 \times 10^{17}$  ions/cm<sup>2</sup>, whereas an angle was 30° concerning the surface. For the second type of experiment, the ion gun's parameters were optimized for a given energy level, with a sample covered by a mask with several holes in various locations. By focusing the ion beam at a specific energy on a single hole, it proved possible to investigate several energies on the same sample. The fluence was constant at  $1 \times 10^{17}$  ions/cm<sup>2</sup>, whereas the energies analyzed were 0.6 keV, 1 keV, and 2 keV, respectively. The sample was bombarded at an angle of 30° concerning its surface.

### 2.4. Experiments into the Effect of Annealing on the Sputtered Sample

The 2 keV sputtered surfaces were annealed at 800 °C for 1 h, after which the obtained surfaces were systematically analyzed. The energy of 2 keV, as well as the relatively high temperature of 800 °C, were chosen to introduce high reduction to the crystals and measure changes as intensively as possible while ensuring that the parameters were within the framework of those typically used in other surface science experiments.

### 2.5. Sputtering–Annealing Cycles

Sputtering/annealing cycles were performed for the temperature of 800 °C and Ar<sup>+</sup> energy of 2 keV. The annealing time during each cycle was 15 min. The ion fluence introduced during one sputtering was approximately  $8.6 \times 10^{15}$  ions/cm<sup>2</sup>. The morphology, crystallography, and electronic properties were measured systematically after 1, 5, 10, 15, 20, 25, 30, 35, 40, and 50 cleaning cycles.

## 2.6. Oxidation

The crystal which was annealed at 800 °C for one hour was selected for the oxidation experiments. Such temperature, as has been shown elsewhere [43], is high enough to remove organic adsorbates. Furthermore, annealing at such a temperature should also significantly reduce the crystal to make changes that will occur during oxidation more noticeable (as crystals annealed at 750 °C are considered slightly reduced [43]). Oxidation was performed by introducing oxygen gas at the pressure of  $5 \times 10^{-8}$  mbar into the UHV chamber. The oxygen exposure was equal to 1260 Langmuirs. The sample which underwent 50 cleaning cycles was oxidized at room temperature using 310 Langmuirs of oxygen.

## 2.7. Oxygen Getter Influence

The reduction of SrTiO<sub>3</sub> was systematically studied by annealing the crystal at the temperatures of 800 °C, 900 °C, 1000 °C and 1100 °C for one hour. Then, the crystals were oxidized at room temperature by exposing them to approximately 150 Langmuirs of oxygen. Two sets of experiments were conducted at the same temperatures but with one key difference. One sample was composed of a SrTiO<sub>3</sub> crystal placed on top of a silicon crystal, while the other sample was composed of a SrTiO<sub>3</sub> crystal placed on top of a TiO<sub>2</sub> crystal. The strontium titanite crystals were annealed by an alternating current flowing through them and the crystal which they were placed upon. Since heated silicon is an oxygen getter, while titanium dioxide is not, one set of annealing experiments was performed with lowered oxygen partial pressure in the chamber while the other was not.

## 3. Results and Discussion

### 3.1. The Effect of Ar Ion Sputtering on the Work Function of TiO<sub>2</sub>(110) Surface

Sputtering with ions is a common method for influencing the composition and properties of multicomponent samples. In the case of a rutile titanium dioxide (110) surface, 1.3 times more oxygen is removed than titanium [23], which means that chemically, this procedure reduces the crystal and also drastically affects other surface properties.

Sputtering of the titanium dioxide (110) surface leads also to its roughening, with the terraced structure being eventually replaced by grains (Figure 1a). The size of these depends on the applied ion beam fluence, but ultimately, it saturates out at approximately 50 nm [21]. The LEED pattern of such a sputtered surface has no diffraction spots, indicating that no long-range ordering is detected. It had been reported that the ion beam sputtering of rutile (110) surfaces may induce the formation of grains composed of titanium suboxides [21] or even a layer of titanium monoxide [22]. The LEED pattern does not reflect this, however, as there are no diffraction spots.

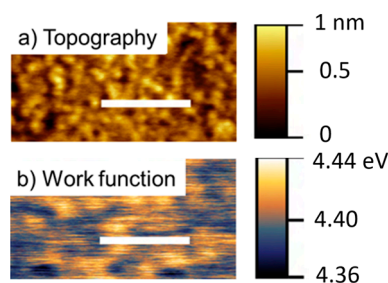


**Figure 1.** (a) The morphology of the sputtered TiO<sub>2</sub>(110) surface (RT, ion energy 2 keV, fluence  $1 \times 10^{17}$  ions cm<sup>-2</sup>) as shown on a KPFM image (scale bar: 200 nm) and (b) the corresponding work function map.

The chemical analysis of the sputtered surface performed using XPS (Figure 2) shows that the surface composition changes from a stoichiometric titanium dioxide to a form that is far from stoichiometric [58]. This indicates that sputtering heavily reduces the surface. Hashimoto et al. [58] in their XPS study thoroughly described the changes in

stoichiometry as a result of sputtering with argon ions, showing at what energies and times of sputtering reduction begins and how effective it is. Their study established the presence of the levelling-off of reduction both as a function of fluence and ion energy. The analysis performed by Rogala et al. proved that this process led to the transformation of the rutile surface into grains of  $Ti_nO_{2n-1}$  Magneli phases stoichiometry [21].

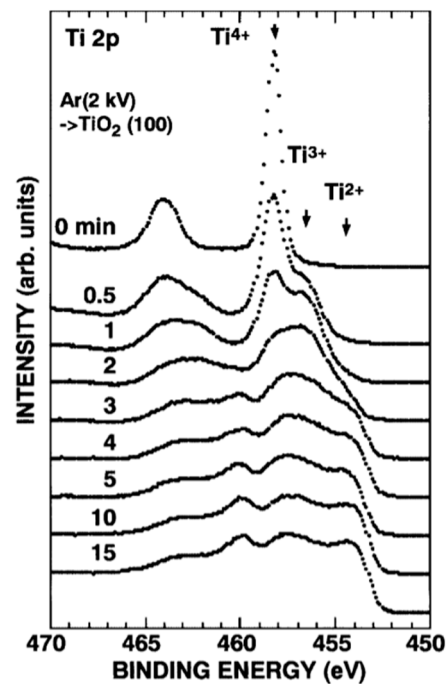


**Figure 2.** XPS spectra showing the evolution of the titanium 2p peak on a rutile (110) surface with increasing time, and therefore fluence, of sputtering. The peaks for each type of titanium ion are marked. Argon ion energy is 2 keV, RT. Reprinted from [58].

Furthermore, the work function of the irradiated surface remains at a level of 4.2 eV, regardless of the fluence used (Figure 3a). The KPFM maps do not show any discerning features, as can be seen in Figure 1b. This is most likely because initially, the surface chemical composition drastically changed, but a further increase in fluence does not change it [21,58]. Sputtering reaches an equilibrium, and the sample is thinned with the surface effectively remaining the same. As the work function is a very surface-related property, even for the relatively small ion beam fluences, the changes in the surface stoichiometry are already drastic. Therefore, it can be presumed that the work function reaches its final value, even for small fluences. The distribution of work functions is narrow; hence, the surface reduces homogeneously, with a little lateral variation of stoichiometry.

The work function (Figure 3b), once again, is approximately the same (3.95(5) eV) regardless of the parameters of sputtering and is explained by the same principle as the results for different fluences. The small differences in values between these two sets of data for sputtered samples are most likely since the first sputtering of the crystal is most sensitive to the starting conditions. Thus, if the as-received crystals differ in some way in the level of impurities, a proper preparation method (such as the cleaning cycles) mitigates the problem as they would be removed from the surface. However, the differences are still noticeable in the case of the first sputtering, especially when using such a surface-sensitive method as KPFM.

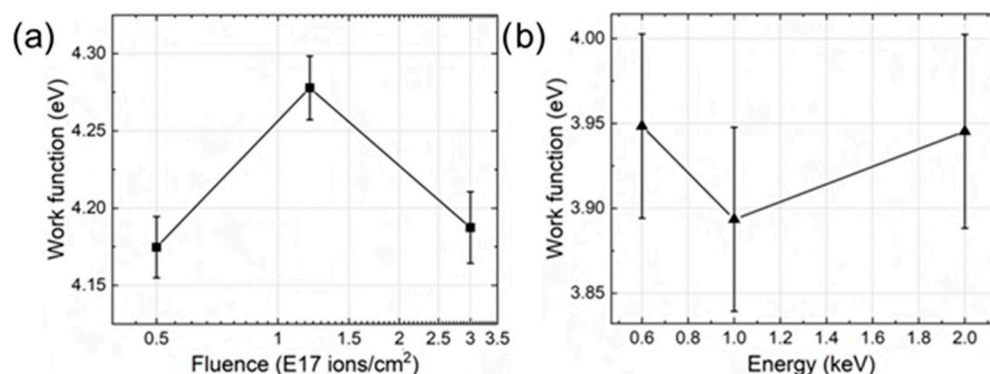


**Figure 3.** The work function of the TiO<sub>2</sub>(110) surface dependence on (a) the applied ion beam fluence of Ar<sup>+</sup> ions (with an energy of 2 keV, RT) and (b) energy of Ar<sup>+</sup> ions (with a fluence of  $1 \times 10^{17}$  ions cm<sup>-2</sup>, RT). Reprinted from [59].

### 3.2. Effect of Annealing on the Work Function of the Ar-Sputtered TiO<sub>2</sub>(110) Surface

Annealing the ion-sputtered TiO<sub>2</sub>(110) surface changes its morphology from a grain-like to a typical terraced structure, as shown in Figure 4. The long-range ordering is also restored, with the LEED pattern becoming visible (see Figure 4d). The diffusion of ions in the crystal is activated by the elevated temperature and a rearrangement of the surface follows. Annealing of such a surface restores its stoichiometry with 4<sup>+</sup> titanium ions once again dominating in the XPS spectra (see Figure 5a).

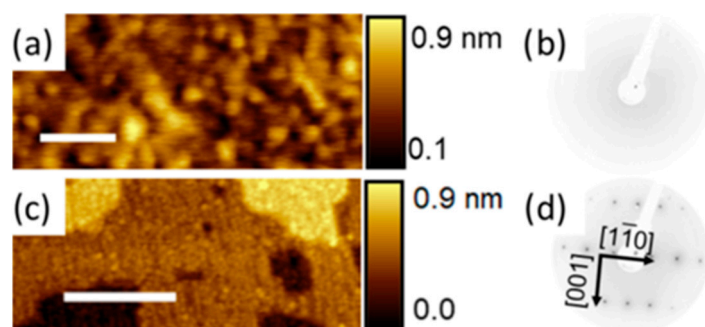


**Figure 4.** (a) Morphology of the sputtered TiO<sub>2</sub>(110) surface (RT, ion energy 2 keV, fluence  $1 \times 10^{17}$  ions cm<sup>-2</sup>) as shown on an AFM image (scale bar: 100 nm) with (b) the corresponding LEED diffraction pattern (energy: 106 eV); (c) the sputtered and annealed (ion energy 2 keV, fluence:  $1.2 \times 10^{17}$  ions cm<sup>-2</sup>, at 800 °C) surface as seen on the STM image (scale bar: 30 nm, sample bias 1.5 V) with (d) the LEED pattern (energy 106 eV). AFM and STM images reprinted from [59].

Changes in the work function follow, with the increase in the surface stoichiometry and crystallographic ordering being reflected in the work function values (see Figure 5b). The change in value is significant, from 4.2 to 4.6 eV. The value of 4.55(5) eV is closer to the reported values of the stoichiometric rutile TiO<sub>2</sub>(110) which range from 5.2 eV [29] to 5.8 eV [33]. As it was shown that with increasing defect density on this surface, the work function decreases [33], it is evident that one act of bombarding and annealing is not enough to achieve a stoichiometric surface. Impurities aggregate on the surface, which sputtering effectively removes.

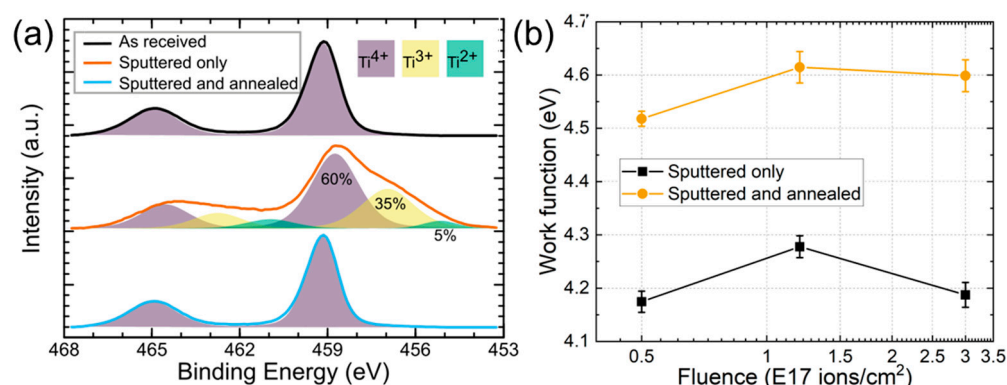


**Figure 5.** (a) The XPS spectra of the as-received  $\text{TiO}_2(110)$ , sputtered only  $\text{TiO}_2(110)$  (ion energy 2 keV, fluence:  $8.0 \times 10^{15}$  ions  $\text{cm}^{-2}$ , RT), and a  $\text{TiO}_2(110)$  surface that was sputtered and subsequently annealed (ion energy 2 keV, fluence:  $8.0 \times 10^{15}$  ions  $\text{cm}^{-2}$ , at 800 °C), (b) Effect of the fluence on the work function for sputtered only (ion energy 2 keV, RT) and sputtered and annealed (ion energy 2 keV, 800 °C)  $\text{TiO}_2(110)$ . Reprinted from [59].

### 3.3. Effect of Sputtering and Annealing on the Work Function of the $\text{TiO}_2(110)$ Surface

Cleaning cycles (CC) can be found in most experimental sections of publications concerning this area of research, but this does not mean that the procedure is the same in all laboratories. An analysis of experimental sections of publications shows that the energies of ions differ (0.6 keV [16], 1 keV [60,61], 2 keV [62,63]) as well as types of ions ( $\text{Ar}^+$  [16],  $\text{Ne}^+$  [64]) and temperatures (527 °C [31,62], 727 °C [65], 1027 °C [16]). This method is so widespread that some publications do not even specify the experimental details, such as the energy of ions [66–68]. The number of cycles used is not a typically specified parameter, as the procedure continues until a sharp LEED diffraction pattern is seen and/or no contaminations on the surface are found using X-ray photoelectron spectroscopy (XPS) [69] or Auger spectroscopy (AES) [70]. To precisely describe the impact of sputtering/annealing cycles on the morphology and stoichiometry of the rutile (110) surface, a prevailing set of parameters was chosen (sputtering: RT,  $\text{Ar}^+$  ions, 2 keV energy, annealing: 800 °C).

Its effects on work function are presented in Figure 6. As can be seen, the work function first increases and then levels out. The value reached a plateau of 4.8(1) eV, which is very close to the lowest reported stoichiometric value of the work function for this surface, which is 5.2 eV [29].

To determine the reason behind this leveling off of the work function values, the coverage of point defects on the surface was noted and plotted as a function of the number of cycles performed on the sample (Figure 7). Since water present in UHV chambers reacts quickly with oxygen vacancies [71], yielding two hydroxyl groups per oxygen defect [71,72], it had been assumed that the bright spots present in images such as the one in Figure 7a are hydroxyl groups. The coverage of oxygen vacancies shown in Figure 7b had been calculated by dividing coverage of hydroxyl groups by two. The coverage value oscillates around 6.5%, which agrees with Wendt et al. [71], who reported that the coverage of oxygen vacancies is around 5% ML for samples with a high number of cleaning cycles performed for 1 keV argon ions and annealing at temperatures between 850 and 950 K. This demonstrates that the surface is no longer reduced after multiple cycles, as the concentration of oxygen vacancies remains the same, regardless of the number of cycles. As the coverage of vacancies is the same on the surface, no matter the number of cleaning cycles, it must mean that the surface is no longer reduced but only the bulk of the crystal. The reason behind the leveling out of the work function must then be the reduced impurity concentration on the surface with an increasing number of cleaning cycles.

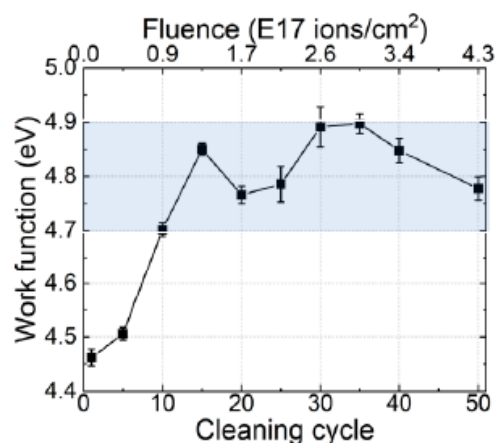


**Figure 6.** Relationship between the work function of TiO<sub>2</sub>(110) and the number of sputtering/annealing cycles that the sample underwent and the total fluence the sample received. The shadow represents the leveling-off value of the work function. The sputtering was performed for argon ions of 2 keV, fluence of  $8.6 \times 10^{15}$  ions cm<sup>-2</sup>, and the subsequent annealing at 800 °C. Reprinted from [59].

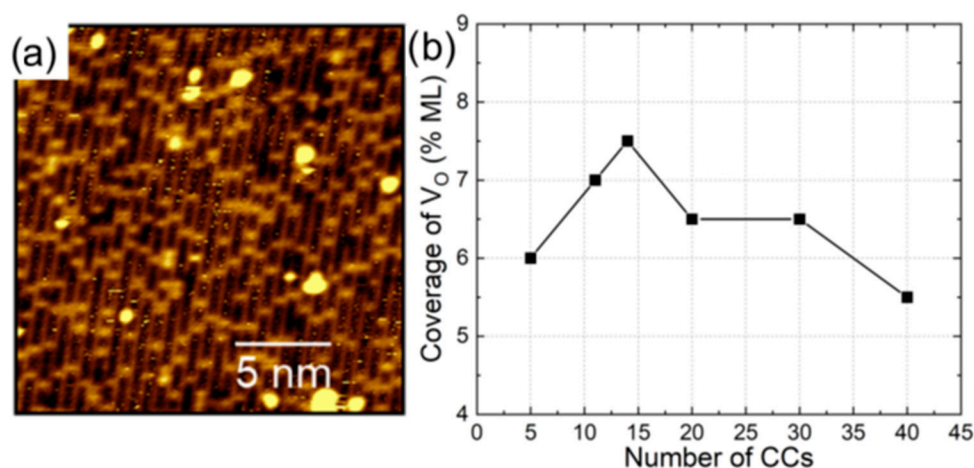


**Figure 7.** (a) Typical STM image of TiO<sub>2</sub>(110) on which the defects coverage calculations were based. This image shows the typical topography of an 11 CCs sample (sample bias 1.7 V and current 11 pA; cycles were composed of sputtering with argon ions of 2 keV, fluence of  $8.6 \times 10^{15}$  ions cm<sup>-2</sup>, and then subsequent annealing at 800 °C); (b) the relationship between the coverage of oxygen vacancies and the number of CC.

### 3.4. Effect of Oxygen Exposure on the Work Function of TiO<sub>2</sub>(110)

To find out if the changes induced by sputtering and annealing are reversible, the crystal was oxidized at room temperature. The work function of the RT-oxygen-exposed sample increases from 4.8(1) to 5.0(3) eV (see Figure 8), which brings it even closer to the values observed for stoichiometric TiO<sub>2</sub>, i.e., from 5.2 eV [29] and 5.8 eV [33]. This indicates that the surface became more stoichiometric, and fewer oxygen vacancies are present as compared to the 50 CCs surface.

Reduction and oxidation are in theory completely reversible processes. In order to check if a simple thermal reduction at 800 °C could be reversed, such a surface was prepared and then oxidized at room temperature in UHV. The work function of a TiO<sub>2</sub>(110) annealed at 800 °C changed after oxygen exposure, which can be seen in Figure 9. The increase was by 0.34(4) eV, which is more than the increase observed by [73], i.e., 0.1 eV; however, the sample used in that research was annealed at a temperature lower by 50 °C, and therefore, it was less reduced and consequently less impacted by oxidation. The value of the work function rises to a value higher than the work function for 700 °C, but it is still far from the

value observed for stoichiometric rutile (110) surfaces, which ranges between 5.2 eV [29] and 5.8 eV [33].

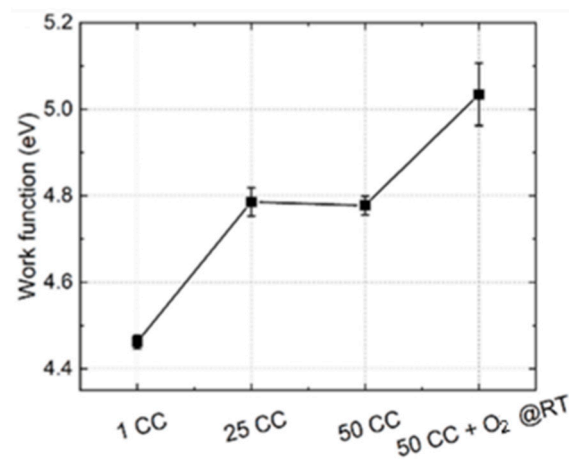


**Figure 8.** The effect of oxidation at RT on the work function of rutile TiO<sub>2</sub>(110) which underwent multiple cleaning cycles. Cycles were composed of sputtering with argon ions of 2 keV, fluence of  $8.6 \times 10^{15}$  ions cm<sup>-2</sup>, and then subsequent annealing at 800 °C. Oxidation proceeded at RT with 310 Langmuirs of oxygen. Reprinted from [59].

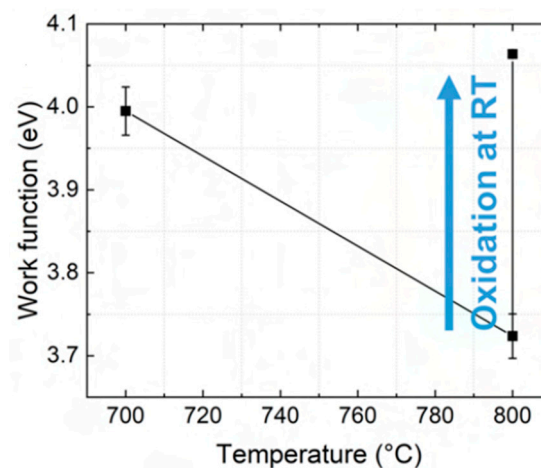


**Figure 9.** The changes in the rutile TiO<sub>2</sub>(110) work function for crystals annealed in UHV at 700 °C and then 800 °C and subsequently oxidized at room temperature in UHV (oxygen exposure equal to 1260 Langmuirs).

The observed changes in electronic properties could be due to the oxidation of the reduced TiO<sub>2</sub> or to an oxidation reaction with impurities. The fact that the experiment was conducted at RT suggests that the changes are most likely due to the healing of oxygen vacancies, which occurs at temperatures above 120 K [37]. It seems unlikely that new oxide phases based on impurities would form at such low temperatures. The fact that the work function value did not reach the values measured for stoichiometric TiO<sub>2</sub> suggests that room temperature oxidation is insufficient to restore the stoichiometry of the surface, which had been reported elsewhere [17,38].

### 3.5. Effect of Oxygen-Gaining Presence on the Work Function of SrTiO<sub>3</sub>(001)

One factor that can significantly affect the thermal reduction process of the metal oxide crystals is the oxygen partial pressure. This can be varied by simply pumping down the system or using reducing agents such as H<sub>2</sub>/Ar mixtures. To reach severely reducing conditions, a method called Extremely Low Oxygen partial Pressure (ELOP) was introduced [57]. It requires the presence of oxygen-getter substances during annealing. The

process of the extreme reduction in the oxygen partial pressure may ultimately lead even to the formation of new oxide phases, as shown in the example of annealing of SrTiO<sub>3</sub> [74,75]. The investigation into the morphology of the SrTiO<sub>3</sub> surface annealed at temperatures up to 1100 °C showed that the surface remains flat regardless if the annealing is completed in the presence of a getter material or not (see Figure 10). The oxygen partial pressure, which is influenced by the getter, does, however, affect the character of the surface obtained. As can be seen in Figure 10, annealing strontium titanate in the presence of pure silicon leads to large terraces with straight edges, while annealing it in the presence of titanium dioxide leads to smaller terraces of less compact edges.

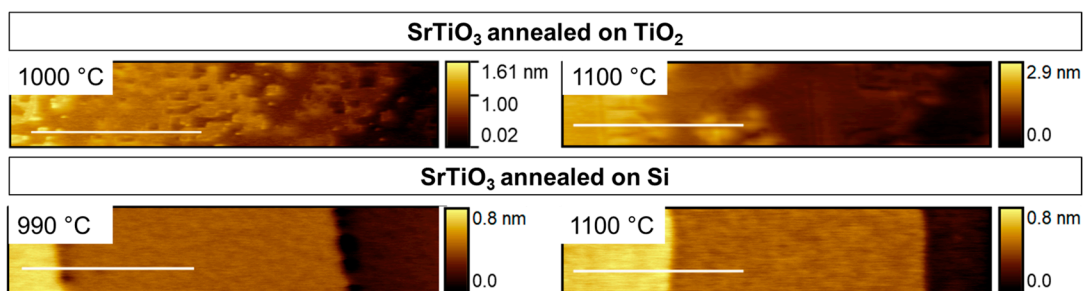


**Figure 10.** The KPFM morphology of SrTiO<sub>3</sub> surfaces annealed at 1000 °C and 1100 °C for crystals annealed in the presence of a non-getter (TiO<sub>2</sub>) and an oxygen-getter material (Si). The scale bar represents 400 nm.

The LEED investigations show that even though the overall morphology of the surfaces does not change drastically depending on the presence of getter material, the arrangement of the atoms of the surface does. As can be seen in Figure 11, depending on the presence or not of an oxygen getter—that is, on the partial pressure of oxygen—different reconstructions are reached at the same annealing temperatures. The SrTiO<sub>3</sub>(001) sample, which was annealed at a higher oxygen partial pressure, that is without a getter, had a (1 × 1) LEED pattern at all studied temperatures, even 1100 °C. In contrast, the sample that was annealed at a lower oxygen partial pressure, namely the getter, went through a whole series of reconstructions at these temperatures. It also starts with a (1 × 1) pattern at 800 °C, but then at 900 °C, it changes into (2 × 2), which at 990 °C changes into c(2 × 2), and finally evolves into ( $\sqrt{13} \times \sqrt{13}$  R33.7°) at 1100 °C. The (2 × 2) reconstruction had been observed at 950 °C [76] and 1000 °C [77], whereas c(2 × 2) was observed at 800 °C [78], ( $\sqrt{13} \times \sqrt{13}$  R33.7°) at 1000 °C [11], and at 1050 °C [79].

To check if the differences in the progression of reconstructions in Figure 11 were due to different levels of reduction (oxygen vacancy formation), their response to oxygen exposure was tested. The reconstruction of the first sample was not affected by the exposure, whereas the reconstruction of the sample annealed on a silicon getter was affected by the exposure, as it can be seen in Figure 12. The diffraction spots of the ( $\sqrt{13} \times \sqrt{13}$  R33.7°) reconstruction almost completely disappeared, and those of the stoichiometric (1 × 1) pattern were predominant. This shows that the additional spots were due to the reduction in the crystal, as they disappear when the sample is oxidized. Furthermore, it was shown that above 830 °C, impurities on the surface (001) of SrTiO<sub>3</sub> tend to disappear [80], and so the changes at such high temperatures are unlikely to be due to the presence of impurities.

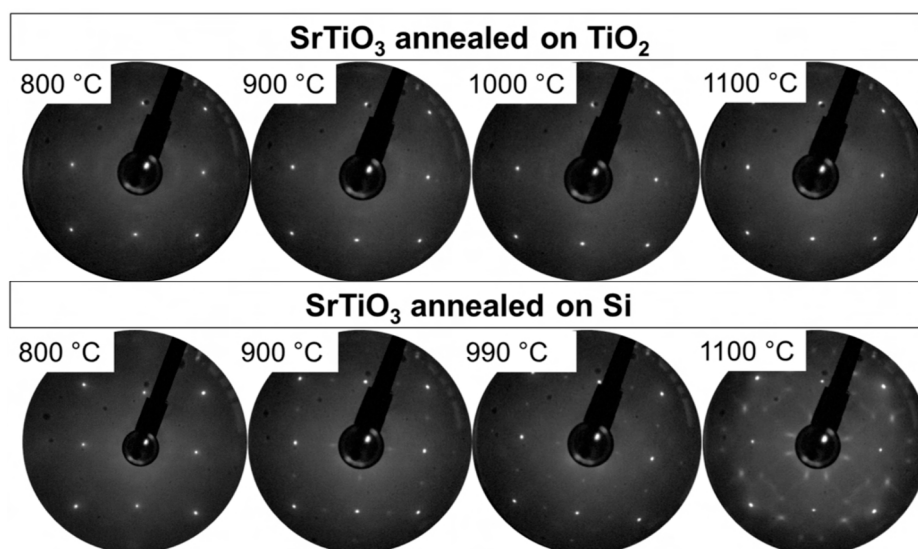


**Figure 11.** Temperature-dependent changes in the SrTiO<sub>3</sub>(001) surface crystallography when annealed in the presence of a non-getter (TiO<sub>2</sub>) and an oxygen-getter material (Si). LEED patterns were made for 106 eV. The Si or TiO<sub>2</sub> crystals were used as a heater in a sandwiched sample mount for direct current heating.

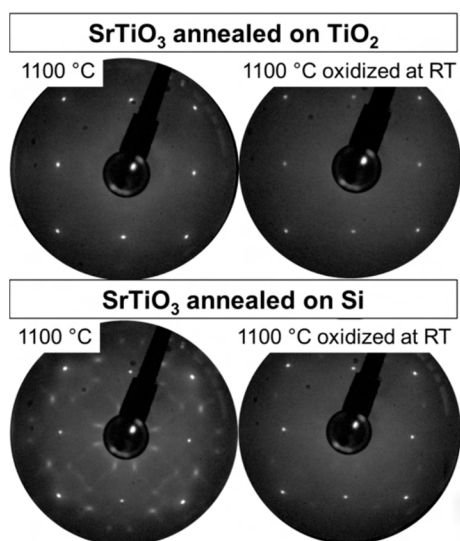


**Figure 12.** The LEED pattern changed after exposure to oxygen (approximately 150 Langmuirs) in the UHV at the RT for a SrTiO<sub>3</sub>(001) surface previously annealed on TiO<sub>2</sub> and one annealed on Si. The electron energy is equal to 106 eV.

The work function of the surfaces annealed in the presence or absence of a silicon getter differs, as can be seen in Figure 13. Both surfaces have work functions at approximately the same value, which is the reported value for a SrTiO<sub>3</sub>(001) with a mostly TiO<sub>2</sub>-terminated (1 × 1) surface annealed at 800 °C (3.75 eV) [11]. The reported value for a stoichiometric TiO<sub>2</sub>-terminated SrTiO<sub>3</sub> is 4.2 eV [81] or 4.3 eV [82], which is higher than the values observed here. The difference is caused by the reduction, as it lowers the work function [83]. The surface that was annealed with a getter exhibited a sudden drop in the value of the work function with increasing temperatures. This is most likely due to the increase in the coverage of oxygen vacancies on the surfaces and subsequent reconstruction, as DFT calculations show that introducing 25% of oxygen vacancies causes a decrease in the work function by 1.5 eV [83]. Moreover, the work function for strontium titanate annealed at 1100 °C corresponds to the previously published value [84]. The experiments show a

general trend in which reduction leads to a decrease in work function, in contrast to DFT simulations, which indicate that the reconstructions observed in this experiment should increase the work function by 1–2 eV [83].

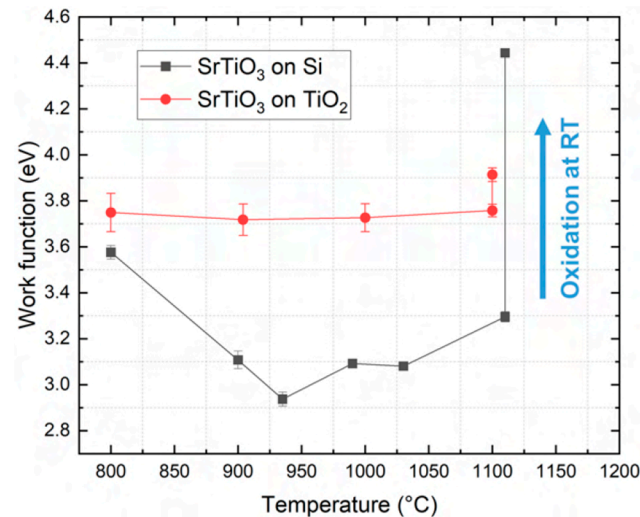


**Figure 13.** Relationship between the work function and annealing temperature for SrTiO<sub>3</sub>, which was annealed on an oxygen-getter material Si and a non-getter material TiO<sub>2</sub> and subsequently oxidized with approximately 150 Langmuirs of oxygen at room temperature in situ.

#### 4. Conclusions

The processes investigated in this paper can be considered as means of inducing a change in the crystals by affecting the equilibrium concentration of oxygen vacancies. During reduction, oxygen vacancy formation is induced, whereas during oxidation, vacancy annihilation is triggered. This is accompanied by the in-plane and out-of-plane diffusion of various species. These changes occur, first and foremost, on the surface, but given appropriate conditions, changes can occur more deeply in the sub-surface region. Extensive changes in the work function were brought about. The changes in the equilibrium conditions led to the movement of atoms and in turn the segregation of impurities and the rearrangement of atoms on the surface. Some of the changes were reversed by exposing the crystals to oxygen, as the latter was incorporated into the reduced crystal.

All of this demonstrates that redox processes can be used to modify transition metal oxides in their composition, crystal structure, and electronic properties as exemplified by the work function evolution. This way, oxides can be tuned to make them suitable for a variety of experiments and applications. It is hoped that this publication can be used as a roadmap by other researchers investigating the redox processes at the nanoscale.

**Funding:** This research was funded by Polish National Science Centre, grant number UMO-2018/29/B/ST5/01406 and the Strategic Programme Excellence Initiative at Jagiellonian University. RSM/7/CK.

**Data Availability Statement:** The data presented in this study are available in articles [58,59] and the PhD dissertation of Karol Cieslik (available on request to the corresponding author).

**Acknowledgments:** We would like to thank Christopher Wood for proofreading the manuscript.

**Conflicts of Interest:** The authors declare no conflict of interest.

## References

1. Almora, O.; Gerling, L.G.; Voz, C.; Alcubilla, R.; Puigdollers, J.; Garcia-Belmonte, G. Superior performance of V<sub>2</sub>O<sub>5</sub> as hole selective contact over other transition metal oxides in silicon heterojunction solar cells. *Sol. Energy Mater. Sol. Cells* **2017**, *168*, 221–226. [[CrossRef](#)]
2. Neophytou, M.; De Bastiani, M.; Gasparini, N.; Aydin, E.; Ugur, E.; Seitkhan, A.; Moruzzi, F.; Choiae, Y.; Ramadan, A.J.; Troughton, J.R.; et al. Enhancing the Charge Extraction and Stability of Perovskite Solar Cells Using Strontium Titanate (SrTiO<sub>3</sub>) Electron Transport Layer. *ACS Appl. Energy Mater.* **2019**, *2*, 8090–8097. [[CrossRef](#)]
3. Mahmoudi, T.; Wang, Y.; Hahn, Y. SrTiO<sub>3</sub>/Al<sub>2</sub>O<sub>3</sub>-Graphene Electron Transport Layer for Highly Stable and Efficient Composites-Based Perovskite Solar Cells with 20.6% Efficiency. *Adv. Energy Mater.* **2019**, *10*, 1903369. [[CrossRef](#)]
4. Haidry, A.A.; Ebach-Stahl, A.; Saruhan, B. Effect of Pt/TiO<sub>2</sub> interface on room temperature hydrogen sensing performance of memristor type Pt/TiO<sub>2</sub>/Pt structure. *Sens. Actuators B Chem.* **2017**, *253*, 1043–1054. [[CrossRef](#)]
5. Znad, H.; Ang, M.H.; Tade, M.O. Ta/Ti- and Nb/Ti-Mixed Oxides as Efficient Solar Photocatalysts: Preparation, Characterization, and Photocatalytic Activity. *Int. J. Photoenergy* **2012**, *2012*, 548158. [[CrossRef](#)]
6. Fujishima, A.; Rao, T.N.; Tryk, D.A. Titanium dioxide photocatalysis. *J. Photochem. Photobiol. C Photochem. Rev.* **2000**, *1*, 39–41. [[CrossRef](#)]
7. Townsend, T.K.; Browning, N.D.; Osterloh, F.E. Nanoscale Strontium Titanate Photocatalysts for Overall Water Splitting. *ACS Nano* **2012**, *6*, 7420–7426. [[CrossRef](#)] [[PubMed](#)]
8. Miyoshi, A.; Nishioka, S.; Maeda, K. Water Splitting on Rutile TiO<sub>2</sub>-Based Photocatalysts. *Chem.—A Eur. J.* **2018**, *24*, 18204–18219. [[CrossRef](#)] [[PubMed](#)]
9. Simanjuntak, F.M.; Ohno, T.; Chandrasekaran, S.; Tseng, T.-Y.; Samukawa, S. Neutral oxygen irradiation enhanced forming-less ZnO-based transparent analog memristor devices for neuromorphic computing applications. *Nanotechnology* **2020**, *31*, 26LT01. [[CrossRef](#)]
10. Li, Y.; Wang, Z.; Midya, R.; Xia, Q.; Yang, J.J. Review of memristor devices in neuromorphic computing: Materials sciences and device challenges. *J. Phys. D Appl. Phys.* **2018**, *51*, 503002. [[CrossRef](#)]
11. Wrana, D.; Rodenbücher, C.; Belza, W.; Szot, K.; Krok, F. In situ study of redox processes on the surface of SrTiO<sub>3</sub> single crystals. *Appl. Surf. Sci.* **2018**, *432*, 46–52. [[CrossRef](#)]
12. Göpel, W.; Anderson, J.; Frankel, D.; Jaehnig, M.; Phillips, K.; Schäfer, J.; Rocker, G. Surface defects of TiO<sub>2</sub>(110): A combined XPS, XAES AND ELS study. *Surf. Sci.* **1984**, *139*, 333–346. [[CrossRef](#)]
13. Rodenbücher, C.; Meuffels, P.; Bihlmayer, G.; Speier, W.; Du, H.; Schwedt, A.; Breuer, U.; Jia, C.-L.; Mayer, J.; Waser, R.; et al. Electrically controlled transformation of memristive titanates into mesoporous titanium oxides via incongruent sublimation. *Sci. Rep.* **2018**, *8*, 3774. [[CrossRef](#)] [[PubMed](#)]
14. Smith, D.J.; McCartney, M.; Bursill, L. The electron-beam-induced reduction of transition metal oxide surfaces to metallic lower oxides. *Ultramicroscopy* **1987**, *23*, 299–303. [[CrossRef](#)]
15. Andronic, L.; Enesca, A. Black TiO<sub>2</sub> Synthesis by Chemical Reduction Methods for Photocatalysis Applications. *Front. Chem.* **2020**, *8*, 565489. [[CrossRef](#)]
16. Bowker, M.; Bennett, R.A. The role of Ti<sup>3+</sup> interstitials in TiO<sub>2</sub>(110) reduction and oxidation. *J. Phys. Condens. Matter* **2010**, *22*, 059801. [[CrossRef](#)]
17. Rogala, M.; Bihlmayer, G.; Dabrowski, P.; Rodenbücher, C.; Wrana, D.; Krok, F.; Klusek, Z.; Szot, K. Self-reduction of the native TiO<sub>2</sub>(110) surface during cooling after thermal annealing—In-operando investigations. *Sci. Rep.* **2019**, *9*, 12563. [[CrossRef](#)]
18. Bak, T.; Nowotny, J.; Nowotny, M.K.; Sheppard, L.R. Defect engineering of titanium dioxide. *J. Aust. Ceram. Soc.* **2008**, *44*, 63–67.
19. Jany, B.; Szajna, K.; Nikiel, M.; Wrana, D.; Trynkiewicz, E.; Pedrys, R.; Krok, F. Energy dependence of nanopillars formation on InSb semiconductor surfaces under gallium FIB and noble gas ions beam irradiation. *Appl. Surf. Sci.* **2015**, *327*, 86–92. [[CrossRef](#)]
20. Serruys, Y.; Ruault, M.-O.; Trocellier, P.; Henry, S.; Kaïtasov, O.; Trouslard, P. Multiple ion beam irradiation and implantation: JANNUS project. *Nucl. Instrum. Methods Phys. Res. Sect. B Beam Interact. Mater. Atoms* **2005**, *240*, 124–127. [[CrossRef](#)]
21. Rogala, M.; Klusek, Z.; Rodenbücher, C.; Waser, R.; Szot, K. Quasi-two-dimensional conducting layer on TiO<sub>2</sub>(110) introduced by sputtering as a template for resistive switching. *Appl. Phys. Lett.* **2013**, *102*, 131604. [[CrossRef](#)]
22. Pabón, B.; Beltrán, J.; Sánchez-Santolino, G.; Palacio, I.; López-Sánchez, J.; Rubio-Zuazo, J.; Rojo, J.; Ferrer, P.; Mascaraque, A.; Muñoz, M.; et al. Formation of titanium monoxide (001) single-crystalline thin film induced by ion bombardment of titanium dioxide (110). *Nat. Commun.* **2015**, *6*, 6147. [[CrossRef](#)] [[PubMed](#)]
23. Lusvardi, V.; Barteau, M.; Chen, J.; Eng, J.; Frühberger, B.; Tepyakov, A. An NEXAFS investigation of the reduction and reoxidation of TiO<sub>2</sub>(001). *Surf. Sci.* **1998**, *397*, 237–250. [[CrossRef](#)]
24. Bennett, R.A. The re-oxidation of the substoichiometric TiO<sub>2</sub>(110) surface in the presence of crystallographic shear planes. *PhysChemComm* **2000**, *3*, 9–14. [[CrossRef](#)]
25. Kashiwaya, S.; Morasch, J.; Streibel, V.; Toupance, T.; Jaegermann, W.; Klein, A. The Work Function of TiO<sub>2</sub>. *Surfaces* **2018**, *1*, 73–89. [[CrossRef](#)]
26. Onishi, H.; Iwasawa, Y. Dynamic Visualization of a Metal-Oxide-Surface/Gas-Phase Reaction: Time-Resolved Observation by Scanning Tunneling Microscopy at 800 K. *Phys. Rev. Lett.* **1996**, *76*, 791–794. [[CrossRef](#)]
27. Li, M.; Hebenstreit, W.; Gross, L.; Diebold, U.; Henderson, M.; Jennison, D.; Schultz, P.; Sears, M. Oxygen-induced restructuring of the TiO<sub>2</sub>(110) surface: A comprehensive study. *Surf. Sci.* **1999**, *437*, 173–190. [[CrossRef](#)]

28. Gorai, P.; Hollister, A.G.; Pangan-Okimoto, K.; Seebauer, E.G. Kinetics of oxygen interstitial injection and lattice exchange in rutile TiO<sub>2</sub>. *Appl. Phys. Lett.* **2014**, *104*, 191602. [[CrossRef](#)]
29. Schierbaum, K.; Fischer, S.; Torquemada, M.; de Segovia, J.; Román, E.; Martín-Gago, J. The interaction of Pt with TiO<sub>2</sub>(110) surfaces: A comparative XPS, UPS, ISS, and ESD study. *Surf. Sci.* **1996**, *345*, 261–273. [[CrossRef](#)]
30. Lo, W.J.; Chung, Y.W.; Somorjai, G.A. Electron spectroscopy studies of the chemisorption of O<sub>2</sub>, H<sub>2</sub> and H<sub>2</sub>O on the TiO<sub>2</sub>(100) surfaces with varied stoichiometry: Evidence for the photogeneration of Ti<sup>3+</sup> and for its importance in chemisorption. *Surf. Sci.* **1978**, *71*, 199–219.
31. Borodin, A.; Reichling, M. Characterizing TiO<sub>2</sub>(110) surface states by their work function. *Phys. Chem. Chem. Phys.* **2011**, *13*, 15442–15447. [[CrossRef](#)] [[PubMed](#)]
32. Onishi, H.; Aruga, T.; Egawa, C.; Iwasawa, Y. Adsorption of CH<sub>3</sub>OH, HCOOH and SO<sub>2</sub> on TiO<sub>2</sub>(110) and stepped TiO<sub>2</sub>(441) surfaces. *Surf. Sci.* **1988**, *193*, 33–46. [[CrossRef](#)]
33. Onda, K.; Li, B.; Petek, H. Two-photon photoemission spectroscopy of TiO<sub>2</sub>(110) surfaces modified by defects and O<sub>2</sub> or H<sub>2</sub>O adsorbates. *Phys. Rev. B* **2004**, *70*, 045415. [[CrossRef](#)]
34. Imanishi, A.; Tsuji, E.; Nakato, Y. Dependence of the Work Function of TiO<sub>2</sub> (Rutile) on Crystal Faces, Studied by a Scanning Auger Microprobe. *J. Phys. Chem. C* **2007**, *111*, 2128–2132. [[CrossRef](#)]
35. Schultz, T.; Lenz, T.; Kotadiya, N.; Heimel, G.; Glasser, G.; Berger, R.; Blom, P.W.M.; Amsalem, P.; de Leeuw, D.M.; Koch, N. Reliable Work Function Determination of Multicomponent Surfaces and Interfaces: The Role of Electrostatic Potentials in Ultraviolet Photoelectron Spectroscopy. *Adv. Mater. Interfaces* **2017**, *4*, 1700324. [[CrossRef](#)]
36. Kowalczyk, D.A.; Rogala, M.; Szałowski, K.; Belić, D.; Dąbrowski, P.; Krukowski, P.; Lutsyk, I.; Piskorski, M.; Nadolska, A.; Krempniński, P.; et al. Two-Dimensional Crystals as a Buffer Layer for High Work Function Applications: The Case of Monolayer MoO<sub>3</sub>. *ACS Appl. Mater. Interfaces* **2022**, *14*, 44506–44515. [[CrossRef](#)]
37. Lira, E.; Hansen, J.; Huo, P.; Bechstein, R.; Galliker, P.; Lægsgaard, E.; Hammer, B.; Wendt, S.; Besenbacher, F. Dissociative and molecular oxygen chemisorption channels on reduced rutile TiO<sub>2</sub>(110): An STM and TPD study. *Surf. Sci.* **2010**, *604*, 1945–1960. [[CrossRef](#)]
38. Wendt, S.; Sprunger, P.T.; Lira, E.; Madsen, G.K.H.; Li, Z.; Hansen, J.; Matthiesen, J.; Blekinge-Rasmussen, A.; Lægsgaard, E.; Hammer, B.; et al. The Role of Interstitial Sites in the Ti3d Defect State in the Band Gap of Titania. *Science* **2008**, *320*, 1755–1759. [[CrossRef](#)]
39. Thomas, A.G.; Flavell, W.R.; Mallick, A.K.; Kumarasinghe, A.R.; Tsoutsou, D.; Khan, N.; Chatwin, C.; Rayner, S.; Smith, G.C.; Stockbauer, R.L.; et al. Comparison of the electronic structure of anatase and rutile TiO<sub>2</sub> single-crystal surfaces using resonant photoemission and x-ray absorption spectroscopy. *Phys. Rev. B* **2007**, *75*, 035105. [[CrossRef](#)]
40. Setvín, M.; Daniel, B.; Mansfeldova, V.; Kavan, L.; Scheiber, P.; Fidler, M.; Schmid, M.; Diebold, U. Surface preparation of TiO<sub>2</sub> anatase (101): Pitfalls and how to avoid them. *Surf. Sci.* **2014**, *626*, 61–67. [[CrossRef](#)]
41. Zhang, L.; Li, M.; Diebold, U. Characterization of Ca impurity segregation on the TiO<sub>2</sub>(110) surface. *Surf. Sci.* **1998**, *412–413*, 242–251. [[CrossRef](#)]
42. Samoylov, A.M.; Popov, V.N. *Titanium Dioxide (TiO<sub>2</sub>) and Its Applications*; Elsevier: Amsterdam, The Netherlands, 2021. [[CrossRef](#)]
43. Möls, K.; Aarik, L.; Mändar, H.; Kasikov, A.; Niilisk, A.; Rammula, R.; Aarik, J. Influence of phase composition on optical properties of TiO<sub>2</sub>: Dependence of refractive index and band gap on formation of TiO<sub>2</sub>-II phase in thin films. *Opt. Mater.* **2019**, *96*, 109335. [[CrossRef](#)]
44. Cao, S.; Chan, T.-S.; Lu, Y.-R.; Shi, X.; Fu, B.; Wu, Z.; Li, H.; Liu, K.; Alzuabi, S.; Cheng, P.; et al. Photocatalytic pure water splitting with high efficiency and value by Pt/porous brookite TiO<sub>2</sub> nanoflutes. *Nano Energy* **2020**, *67*, 104287. [[CrossRef](#)]
45. Misawa, K.; Sekine, Y.; Kusukubo, Y.; Sohara, K. Photocatalytic degradation of atmospheric fine particulate matter (PM<sub>2.5</sub>) collected on TiO<sub>2</sub> supporting quartz fibre filter. *Environ. Technol.* **2018**, *41*, 1266–1274. [[CrossRef](#)] [[PubMed](#)]
46. Haider, A.J.; Jameel, Z.N.; Al-Hussaini, I.H. Review on: Titanium Dioxide Applications. *Energy Procedia* **2019**, *157*, 17–29. [[CrossRef](#)]
47. Nassau, K.; Miller, A. Strontium titanate: An index to the literature on properties and the growth of single crystals. *J. Cryst. Growth* **1988**, *91*, 373–381. [[CrossRef](#)]
48. Szot, K.; Speier, W.; Bihlmayer, G.; Waser, R. Switching the electrical resistance of individual dislocations in single-crystalline SrTiO<sub>3</sub>. *Nat. Mater.* **2006**, *5*, 312–320. [[CrossRef](#)]
49. Yang, H.; Yan, F.; Lin, Y.; Wang, T. Novel Strontium Titanate-Based Lead-Free Ceramics for High-Energy Storage Applications. *ACS Sustain. Chem. Eng.* **2017**, *5*, 10215–10222. [[CrossRef](#)]
50. Pervez, N.K.; Hansen, P.J.; York, R.A. High tunability barium strontium titanate thin films for rf circuit applications. *Appl. Phys. Lett.* **2004**, *85*, 4451. [[CrossRef](#)]
51. Shibuya, K.; Ohnishi, T.; Kawasaki, M.; Koinuma, H.; Lippmaa, M.L.M. Metallic LaTiO<sub>3</sub>/SrTiO<sub>3</sub> Superlattice Films on the SrTiO<sub>3</sub>(100) Surface. *Jpn. J. Appl. Phys.* **2004**, *43*, L1178. [[CrossRef](#)]
52. Singh, R.K.; Narayan, J.; Singh, A.K.; Krishnaswamy, J. In situ processing of epitaxial Y-Ba-Cu-O high T<sub>c</sub> superconducting films on (100) SrTiO<sub>3</sub> and (100) YS-ZrO<sub>2</sub> substrates at 500–650 °C. *Appl. Phys. Lett.* **1989**, *54*, 2271–2273. [[CrossRef](#)]
53. Aschauer, U.; Spaldin, N.A. Competition and cooperation between antiferrodistortive and ferroelectric instabilities in the model perovskite SrTiO<sub>3</sub>. *J. Phys. Condens. Matter* **2014**, *26*, 122203. [[CrossRef](#)]

54. Merkle, R.; Maier, J. How Is Oxygen Incorporated into Oxides? A Comprehensive Kinetic Study of a Simple Solid-State Reaction with SrTiO<sub>3</sub> as a Model Material. *Angew. Chem. Int. Ed.* **2008**, *47*, 3874–3894. [[CrossRef](#)]
55. Szot, K.; Rodenbücher, C.; Bihlmayer, G.; Speier, W.; Ishikawa, R.; Shibata, N.; Ikuhara, Y. Influence of Dislocations in Transition Metal Oxides on Selected Physical and Chemical Properties. *Crystals* **2018**, *8*, 241. [[CrossRef](#)]
56. Mansfeldova, V.; Zlamalova, M.; Tarabkova, H.; Janda, P.; Vorokhta, M.; Piliai, L.; Kavan, L. Work Function of TiO<sub>2</sub> (Anatase, Rutile, and Brookite) Single Crystals: Effects of the Environment. *J. Phys. Chem. C* **2021**, *125*, 1902–1912. [[CrossRef](#)]
57. Krok, F.; Kolodziej, J.; Such, B.; Czuba, P.; Struski, P.; Piatkowski, P.; Szymonski, M. Dynamic force microscopy and Kelvin probe force microscopy of KBr film on InSb(001) surface at submonolayer coverage. *Surf. Sci.* **2004**, *566–568*, 63–67. [[CrossRef](#)]
58. Hashimoto, S.; Tanaka, A. Alteration of Ti 2p XPS spectrum for titanium oxide by low-energy Ar ion bombardment. *Surf. Interface Anal.* **2002**, *34*, 262–265. [[CrossRef](#)]
59. Cieřlik, K.; Wrana, D.; Szajna, K.; Beřza, W.; Rogala, M.; Rodenbücher, C.; Dąbczyński, P.; Szot, K.; Krok, F. Tuning the electronic properties of a clean TiO<sub>2</sub>(1 1 0) surface via repeated sputtering and annealing: A KPFM and LC-AFM study. *Appl. Surf. Sci.* **2021**, *571*, 151303. [[CrossRef](#)]
60. Setvin, M.; Hulva, J.; Parkinson, G.S.; Schmid, M.; Diebold, U. Electron transfer between anatase TiO<sub>2</sub> and an O<sub>2</sub> molecule directly observed by atomic force microscopy. *Proc. Natl. Acad. Sci. USA* **2017**, *114*, E2556–E2562. [[CrossRef](#)] [[PubMed](#)]
61. Humphrey, D.S.; Pang, C.L.; Chen, Q.; Thornton, G. Electron induced nanoscale engineering of rutile TiO<sub>2</sub> surfaces. *Nanotechnology* **2018**, *30*, 025303. [[CrossRef](#)] [[PubMed](#)]
62. Du, Y.; Deskins, N.A.; Zhang, Z.; Dohnalek, Z.; Dupuis, M.; Lyubintsky, I. Formation of O adatom pairs and charge transfer upon O<sub>2</sub> dissociation on reduced TiO<sub>2</sub>(110). *Phys. Chem. Chem. Phys.* **2010**, *12*, 6337–6344. [[CrossRef](#)]
63. Katsube, D.; Ojima, S.; Inami, E.; Abe, M. Atomic-resolution imaging of rutile TiO<sub>2</sub>(110)-(1 × 2) reconstructed surface by non-contact atomic force microscopy. *Beilstein J. Nanotechnol.* **2020**, *11*, 443–449. [[CrossRef](#)] [[PubMed](#)]
64. Petrik, N.G.; Kimmel, G.A. Electron- and Hole-Mediated Reactions in UV-Irradiated O<sub>2</sub> Adsorbed on Reduced Rutile TiO<sub>2</sub>(110). *J. Phys. Chem. C* **2010**, *115*, 152–164. [[CrossRef](#)]
65. Yim, C.M.; Pang, C.L.; Thornton, G. Oxygen Vacancy Origin of the Surface Band-Gap State of TiO<sub>2</sub>(110). *Phys. Rev. Lett.* **2010**, *104*, 036806. [[CrossRef](#)]
66. Kim, Y.K.; Hwang, C.-C. Photoemission study on the adsorption of ethanol on clean and oxidized rutile TiO<sub>2</sub>(110)-1 × 1 surfaces. *Surf. Sci.* **2011**, *605*, 2082–2086. [[CrossRef](#)]
67. Sohn, S.-D.; Kim, S.H.; Kwak, S.K.; Shin, H.-J. Defect-associated adsorption of monoethanolamine on TiO<sub>2</sub>(1 1 0): An alternative way to control the work function of oxide electrode. *Appl. Surf. Sci.* **2018**, *467–468*, 1213–1218. [[CrossRef](#)]
68. Zhou, C.; Ma, Z.; Ren, Z.; Mao, X.; Dai, D.; Yang, X. Effect of defects on photocatalytic dissociation of methanol on TiO<sub>2</sub>(110). *Chem. Sci.* **2011**, *2*, 1980–1983. [[CrossRef](#)]
69. Wu, Z.; Xiong, F.; Wang, Z.; Huang, W. Thermal-, photo- and electron-induced reactivity of hydrogen species on rutile TiO<sub>2</sub>(110) surface: Role of oxygen vacancy. *Chin. Chem. Lett.* **2018**, *29*, 752–756. [[CrossRef](#)]
70. Dohnálek, Z.; Kim, J.; Bondarchuk, O.; White, J.M.; Kay, B.D. Physisorption of N<sub>2</sub>, O<sub>2</sub>, and CO on Fully Oxidized TiO<sub>2</sub>(110). *J. Phys. Chem. B* **2006**, *110*, 6229–6235. [[CrossRef](#)]
71. Wendt, S.; Schaub, R.; Matthiesen, J.; Vestergaard, E.; Wahlström, E.; Rasmussen, M.; Thostrup, P.; Molina, L.; Lægsgaard, E.; Stensgaard, I.; et al. Oxygen vacancies on TiO<sub>2</sub>(110) and their interaction with H<sub>2</sub>O and O<sub>2</sub>: A combined high-resolution STM and DFT study. *Surf. Sci.* **2005**, *598*, 226–245. [[CrossRef](#)]
72. Schaub, R.; Thostrup, P.; Lopez, N.; Lægsgaard, E.; Stensgaard, I.; Nørskov, J.K.; Besenbacher, F. Oxygen Vacancies as Active Sites for Water Dissociation on Rutile TiO<sub>2</sub>(110). *Phys. Rev. Lett.* **2001**, *87*, 266104. [[CrossRef](#)] [[PubMed](#)]
73. Rodenbücher, C.; Wrana, D.; Meuffels, P.; Rogala, M.; Krok, F.; Szot, K. Electrical nanopatterning of TiO<sub>2</sub> single crystal surfaces *in situ* via local resistance and potential switching. *APL Mater.* **2018**, *6*, 066105. [[CrossRef](#)]
74. Rodenbücher, C.; Meuffels, P.; Speier, W.; Ermrich, M.; Wrana, D.; Krok, F.; Szot, K. Stability and Decomposition of Perovskite-Type Titanates upon High-Temperature Reduction. *Phys. Status Solidi (RRL)–Rapid Res. Lett.* **2017**, *11*, 1700222. [[CrossRef](#)]
75. Wrana, D.; Rodenbücher, C.; Jany, B.R.; Kryshnal, O.; Cempura, G.; Kruk, A.; Indyka, P.; Szot, K.; Krok, F. A bottom-up process of self-formation of highly conductive titanium oxide (TiO) nanowires on reduced SrTiO<sub>3</sub>. *Nanoscale* **2018**, *11*, 89–97. [[CrossRef](#)] [[PubMed](#)]
76. Silly, F.; Newell, D.T.; Castell, M.R. SrTiO<sub>3</sub>(001) reconstructions: The (2 × 2) to c(4 × 4) transition. *Surf. Sci.* **2006**, *600*, 219–223. [[CrossRef](#)]
77. Kubo, T.; Nozoye, H. Surface structure of SrTiO<sub>3</sub>(100). *Surf. Sci.* **2003**, *542*, 177–191. [[CrossRef](#)]
78. Radovic, M.; Lampis, N.; Granozio, F.M.; Perna, P.; Ristic, Z.; Salluzzo, M.; Schlepütz, C.M.; di Uccio, U.S. Growth and characterization of stable SrO-terminated SrTiO<sub>3</sub> surfaces. *Appl. Phys. Lett.* **2009**, *94*, 022901. [[CrossRef](#)]
79. Kienzle, D.M.; Becerra-Toledo, A.E.; Marks, L.D. Vacant-Site Octahedral Tilings on SrTiO<sub>3</sub>(001), the (sqrt13 × sqrt13)R33.7° Surface, and Related Structures. *Phys. Rev. Lett.* **2011**, *106*, 176102. [[CrossRef](#)]
80. González, M.S.M.; Aguirre, M.H.; Morán, E.; Alario-Franco, M.; Perez-Dieste, V.; Avila, J.; Asensio, M.C. In situ reduction of (100) SrTiO<sub>3</sub>. *Solid State Sci.* **2000**, *2*, 519–524. [[CrossRef](#)]
81. Maus-Friedrichs, W.; Frerichs, M.; Gunhold, A.; Krischok, S.; Kempter, V.; Bihlmayer, G. The characterization of SrTiO<sub>3</sub>(001) with MIES, UPS(HeI) and first-principles calculations. *Surf. Sci.* **2002**, *515*, 499–506. [[CrossRef](#)]

82. Susaki, T.; Makishima, A.; Hosono, H. Work function engineering via LaAlO<sub>3</sub>/SrTiO<sub>3</sub> polar interfaces. *Phys. Rev. B* **2011**, *84*, 115456. [[CrossRef](#)]
83. Ma, T.; Jacobs, R.; Booske, J.; Morgan, D. Understanding the interplay of surface structure and work function in oxides: A case study on SrTiO<sub>3</sub>. *APL Mater.* **2020**, *8*, 071110. [[CrossRef](#)]
84. Wrana, D.; Cieřlik, K.; Belza, W.; Rodenbächer, C.; Szot, K.; Krok, F. Kelvin probe force microscopy work function characterization of transition metal oxide crystals under ongoing reduction and oxidation. *Beilstein J. Nanotechnol.* **2019**, *10*, 1596–1607. [[CrossRef](#)] [[PubMed](#)]

**Disclaimer/Publisher’s Note:** The statements, opinions and data contained in all publications are solely those of the individual author(s) and contributor(s) and not of MDPI and/or the editor(s). MDPI and/or the editor(s) disclaim responsibility for any injury to people or property resulting from any ideas, methods, instructions or products referred to in the content.